Chemical Science

ROYAL SOCIETY OF CHEMISTRY

EDGE ARTICLE

View Article Online
View Journal | View Issue

Cite this: *Chem. Sci.*, 2025, **16**, 18141

All publication charges for this article have been paid for by the Royal Society of Chemistry

Received 9th June 2025
Accepted 1st September 2025

DOI: 10.1039/d5sc04204f

rsc.li/chemical-science

Covalent organic framework catalytic membranes for durable multitasking water purification

Guishan Hu,[a] Binyu Zhou,[a] Yu Zhen,[a] Junyong Zhu, *[a] Jingwei Hou, [b] Yatao Zhang, *[a] Yong Wang *[c] and Bart Van der Bruggend[d]

Heterogeneous catalysis has emerged as a promising approach for sustainable and efficient water purification due to its high catalytic efficacy and low energy consumption. However, the complex nature of nontraditional water resources (*e.g.*, trace toxic metals, organic molecules, and high salinity) leads to gradual catalyst deactivation, hindering large-scale implementation. Here we introduce the concept of sieving-coupled nanoconfined catalytic water pollutant conversion for rapid purification of complex water sources. This dual-function system was achieved by integrating *in situ* recycled palladium nanoclusters within covalent organic framework (COF) membranes. The strong interaction between Pd and the pyrazine nitrogen in the COF facilitates the formation of a Pd layer within a 40 nm-thick COF nanofilm. The resultant Pd^0–TpPz membrane exhibited a high permeability of 85.4 L m^{-2} h^{-1} bar^{-1} while achieving 99.8% for Eriochrome black T. This precise-sieving effect of the membrane enables the efficient catalytic reduction of various pollutants such as rhodamine B (RhB), Cr(VI), and 4-nitroaniline in complex systems. The reported Pd^0–TpPz membrane evinced favorable long-term stability, recyclability, antimicrobial activity, and acid–base resistance (pH = 2–12), demonstrating its high potential for water treatment. This work paves the way towards the development of sieving-coupled nanoconfined catalysis for rapid water purification.

Introduction

Global freshwater resources are dwindling, and the supply of clean water is insufficient, necessitating the urgent development of innovative technologies to harness clean water from alternative sources.[1] Nontraditional water sources, such as wastewater, brackish water, and seawater, offer a promising avenue for addressing global water scarcity.[2] However, these sources are predominantly complex and contaminated with a diverse array of pollutants, including organic dyes, high salinity, trace toxic metals, and other hazardous substances.[3,4] Furthermore, these water sources frequently exhibit elevated levels of biochemical oxygen demand and chemical oxygen demand, coupled with low biodegradability.[5] The specific types and concentrations of pollutants can vary broadly depending on the source and the characteristics of the water.[6] Heterogeneous catalysts have emerged as a powerful tool in water purification due to their excellent catalytic efficiency, environmental friendliness, and mild reaction conditions.[7] However, when applied to complex water environments, these catalysts face several challenges including weakened catalytic activity, limited selectivity, biofouling, and insufficient recycling stability.[8] Therefore, developing multifunctional water treatment technologies for complex water sources remains a critical goal in the field of water remediation.[9]

Membrane-based technologies play a key role in water treatment and purification primarily due to their high selectivity, low cost, and broad applicability.[10–13] Dense ultrafiltration and loose nanofiltration are among the most common membrane-based processes utilized for the fractionation of diverse solutes with varying molecular/ionic sizes.[14,15] However, these approaches are incapable of retaining small toxic molecules and high-valent metals (*e.g.*, 4-NP and Cr^{VI}), necessitating additional costly separation units to remove these contaminants.[16,17] The widespread large-scale application of these technologies is further hindered by the limited physical and chemical tunability of the pore structure in conventional polymeric membranes. Of note, the empirical-dominated processing of common linear polymers frequently yields high packing-density membranes with limited free volume and dynamic porosity, leading to a trade-off between flux and selectivity.[18] Rapid interfacial polymerization of two highly reactive monomers (diamine and triacyl chloride) is effective in fabricating thin selective films but lacks fine control of the membrane microstructure.[19] The resultant wide pore size distribution limits membrane performance and increases the cost of water treatment. While substantial improvements in water

[a]*School of Chemical Engineering, Zhengzhou University, Zhengzhou, 450001, P. R. China. E-mail: zhujunyong@zzu.edu.cn; zhangyatao@zzu.edu.cn*

[b]*School of Chemical Engineering, The University of Queensland, St Lucia, QLD 4072, Australia*

[c]*School of Energy and Environment, Southeast University, Nanjing, 210096, P. R. China. E-mail: yongwang@seu.edu.cn*

[d]*Department of Chemical Engineering, KU Leuven, Celestijnenlaan 200F, B-3001, Leuven, Belgium*

purification membranes have been achieved using optimized film processing strategies, their surface fouling propensity, especially biofouling, is often overlooked.[20–22] Once a mature biofilm forms on the membrane surface, there is a significant decline in membrane performance and lifespan, hindering its practical and large-scale use.[23] In this context, new membrane materials fabricated through molecular-level design methods are crucial for advancing membrane-based water purification technologies.

Unlike traditional linear polymers, covalent organic frameworks (COFs) have emerged as crystalline porous polymers that feature structural periodicity, well-arranged nanopores, high surface area, and robust water stability.[24–26] These properties, combined with their designable pore architectures and tunable apertures, make them promising candidates for selective adsorption and separation applications with a level of precision that is not achievable using conventional materials.[27–29] Furthermore, the unique COF architecture provides confined spaces for the interplay of ions or guest molecules, thus evincing unique properties and functions. Their ordered nanopores offer stable anchoring sites for metal catalysts, ensuring nanoconfined catalytic conversion of small molecules and ions.[30,31] In addition, by tailoring their pore size and functional groups, the dispersion and catalytic activity of metal catalysts can be optimized, thereby enhancing the selectivity and efficiency of the reaction.[32] Importantly, the diversity of building blocks and covalent linkages makes COFs highly promising for selective capture of precious metal catalysts from nontraditional water sources.[33] This unique function enables the usage of precious metal-containing wastewater to upcycle COF catalytic membranes with recycled metal nano-catalysts.[34] More importantly, pore engineering of COF membranes allows them to precisely sieve the organics with large molecular weights, facilitating continuous catalytic conversion of toxic ions and small molecules that can enter the nanopores.[35] Therefore, COFs offer a promising opportunity to leverage precise sieving and heterogeneous catalysis for potentially improved water purification efficiency.[36,37]

To this end, we sought to develop a separation-synergistic catalytic membrane platform for use in multifunctional water-purification applications, based on the introduction of recycled Pd nanoclusters into COF separation membranes. Unlike heterogeneous catalysis using 2D laminar membranes, which may suffer from the fouling of catalytic sites, our proposed nanoconfined membrane reaction platform fully unlocks the advantages of ordered nanopores and chemical tunability. This new mode enables simultaneous rejection of large organic dyes and catalytic conversion of small organics or toxic high-valence metals when dealing with complex wastewater (Fig. 1a). A TpPz-COF membrane was fabricated *in situ* on a Kevlar substrate *via* an IP reaction between 1,3,5-triformylphloroglucinol (Tp) and 1,4-diaminopyrazine (Pz). This pyrazine-based COF membrane exhibited the highest selectivity for the capture of $PdCl_4^{2-}$ from simulated electronic wastewater containing diverse competing ions (Fig. 1b). This is likely due to the high affinity between palladium and dual-nitrogen atoms from the pyrazine-based skeleton. The subsequent *in situ* reduction feasibly transformed the adsorptive membrane into a catalytic COF membrane rich in recycled Pd nanoclusters, without diminishing its original

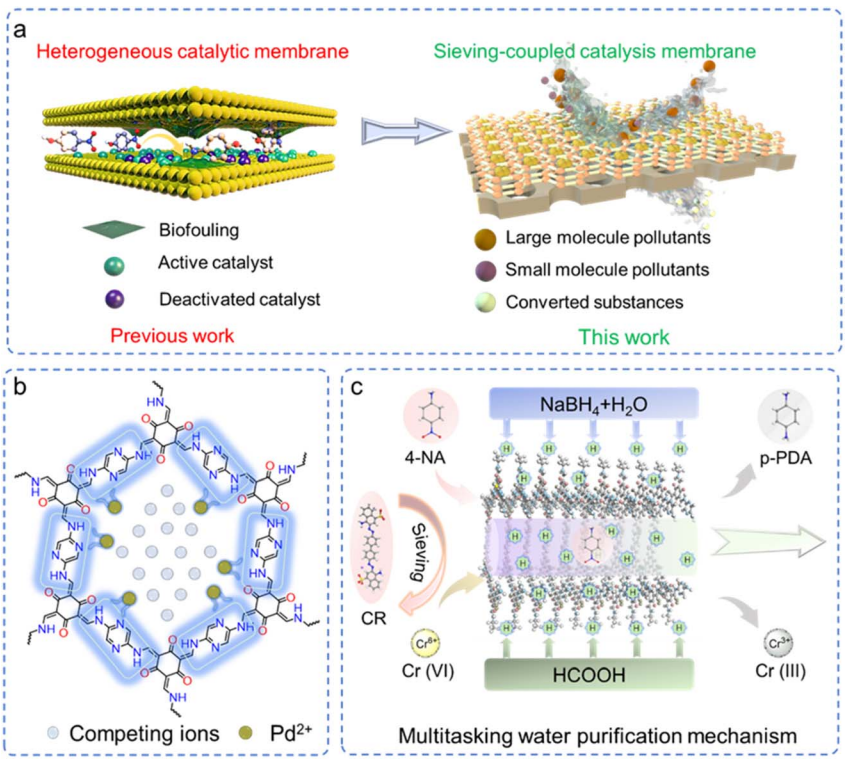

Fig. 1 (a) Comparison of separation synergistic catalytic membranes and heterogeneous catalytic membranes, (b) schematic diagram of capturing Pd^{2+} using TpPz membranes, and (c) schematic diagram of the Pd^0–TpPz separation synergistic catalytic mechanism.

filtration performance. This Pd-appended COF membrane not only exhibited high removal efficiency of large dye molecules (*e.g.*, Congo red, methyl blue, and Direct Red 23) but also enabled catalytic reduction of toxic molecules and high-valence metals (rhodamine B, 4-nitroaniline, methyl orange, 4-nitrophenol, and Cr^{VI}, Fig. 1c). By combining robust long-term stability, recyclability, antimicrobial activity, and acid–base resistance (pH 2–12), this membrane shows great promise for real-world water purification applications.

Results and discussion

Morphology and structure of TpPz nanofilms

A TpPz nanofilm was fabricated *via* an interfacial reaction between Tp and Pz linkers at room temperature. The thin film formed at the free water–oil interface was collected, washed with organic solvents to remove unreacted precursors, and dried under vacuum at 80 °C for 24 hours. The crystal structure of the TpPz nanofilm was determined using powder X-ray diffraction (PXRD, Fig. 2a). The diffraction peaks at $2\theta = 4.80°$, 7.80°, and 27.16° were indexed to the (100), (110), and (001) planes of the AA-stacked TpPz structure, confirmed by simulated XRD patterns. The TpPz nanofilm was utilized to selectively capture $PdCl_4^{2-}$ from simulated electroplating wastewater, followed by fabricating a Pd^0–TpPz film *via in situ* reduction. Compared to TpPz, the PXRD pattern of Pd^0–TpPz showed the retention of the (100) and (001) peaks of TpPz and additional peaks at $2\theta = 40.15°$, 46.71°, 68.13°, 82.12°, and 86.61°, corresponding to the (111), (200), (220), (311), and (222) planes of zero-valent Pd (Fig. S3).[38] High-resolution transmission electron microscopy (HRTEM)

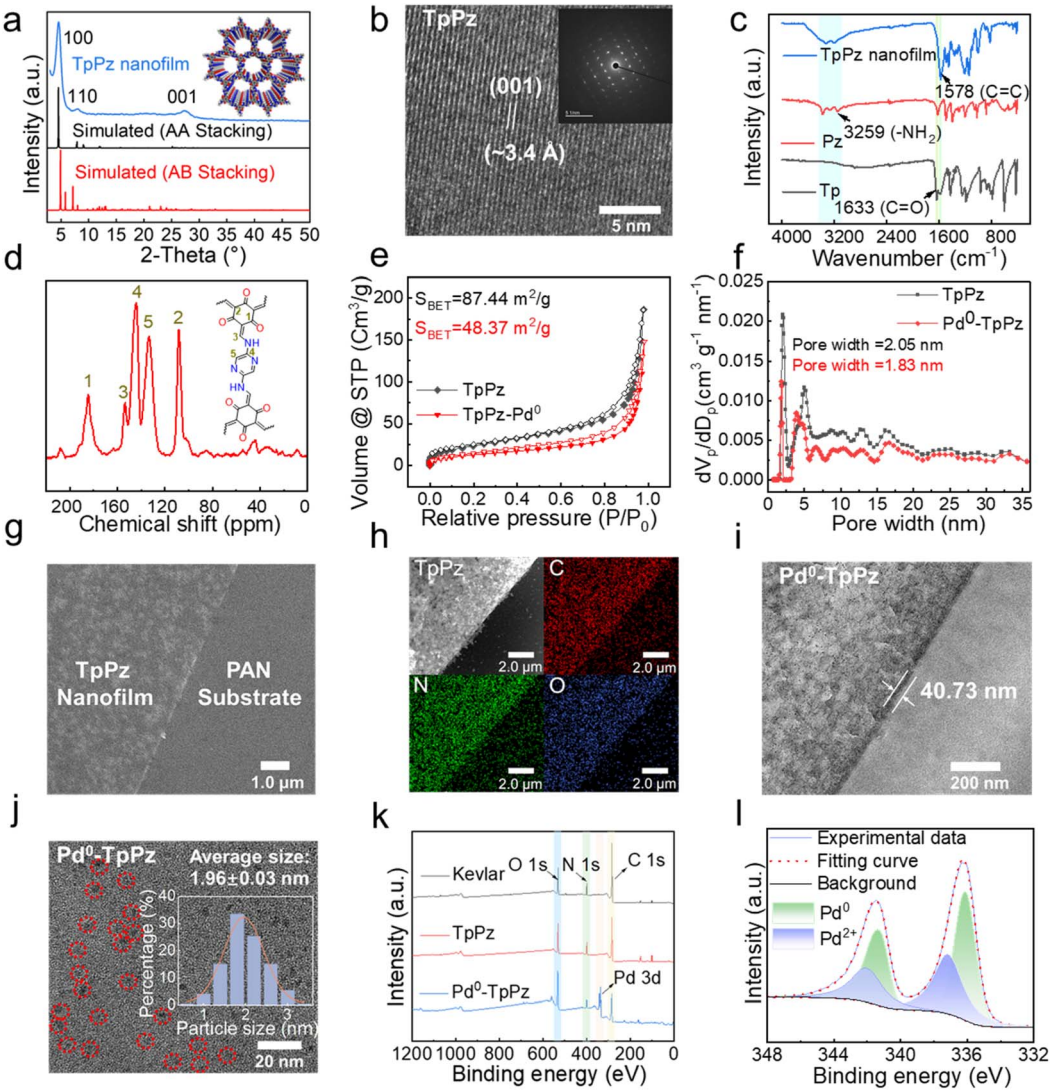

Fig. 2 Characterization of TpPz free-standing nanofilms. (a) PXRD patterns, (b) HRTEM image (inset: SAED pattern), (c) FTIR spectrum, and (d) solid-state NMR spectra of the TpPz nanofilm ($Tp_{0.75}$-$Pz_{4.0}$-24). (e) N_2 sorption isotherms of TpPz and Pd^0–TpPz nanofilm ($Tp_{0.75}$-$Pz_{4.0}$-24); (f) pore widths of the TpPz and Pd^0–TpPz nanofilm ($Tp_{0.75}$-$Pz_{4.0}$-24); (g) SEM image of the surface transfer free-standing film ($Tp_{0.75}$-$Pz_{4.0}$-24) on the surface of a PAN substrate; (h) TEM/EDS mapping image and elemental distributions of the surface transfer free-standing film ($Tp_{0.75}$-$Pz_{4.0}$-24); (i) the cross-sectional high-resolution TEM image of Pd^0–TpPz; (j) the size distribution profile of Pd nanoclusters; (k) XPS spectra of prepared membranes; (l) the Pd 3d spectrum of Pd^0–TpPz membranes measured by XPS.

clearly shows the lattice fringes of the film with a spacing of ~3.4 Å, which represents that the interlayer distance of TpPz monolayers originated from the π–π stacking (Fig. 2b). Besides, clear diffraction rings can also be seen in the selected area electron diffraction (SAED) pattern, further indicating the high crystallinity and anisotropic orientation of the TpPz films (inset of Fig. 2b).

Fourier transform-infrared (FTIR) spectra of organic linkers and TpPz (Fig. 2c) reveal the successful condensation between Tp and Pz linkers. The disappearance of the aldehyde (1633 cm^{-1}) and the amine (3259 cm^{-1}) peaks, coupled with the emergence of a new peak at 1578 cm^{-1} C=C stretching, provides strong evidence for the formation of a β-ketoenamine-linked COF film. Solid-state ^{13}C CP-MAS NMR spectroscopy (Fig. 2d) further elucidates the atomic-level structure of the TpPz nanofilm. The signal at 184 ppm is indicative of keto C=O bond formation, likely resulting from tautomerization during the reaction. The signal at 108 ppm corroborates the presence of C=C–N bonds and further supports the keto structure. In addition, the peak that emerged in the range of 144–153 ppm for the TpPz film is assigned to the C–NH (nonheterocyclic N) carbon, while the signal at ~152 ppm corresponds to the C–N (heterocyclic N) carbon.[39]

Nitrogen sorption isotherms at 77 K confirm the permanent porosity of TpPz and Pd^0–TpPz films. TpPz exhibits a BET surface area of 87.4 $m^2\ g^{-1}$ and a primary pore size of 2.05 nm, consistent with an AA-eclipsed framework geometry (Fig. 2e and f). Pd^0–TpPz shows a reduced BET surface area (48.3 $m^2\ g^{-1}$) and a smaller pore size (1.83 nm), likely due to the significant adsorption of Pd within the pores. In contrast, Pd^0–TpPz displayed a primary pore size of 1.83 nm, likely attributed to the significant adsorption of Pd within the TpPz pores, resulting in a decline in both pore size and BET surface area.[40] Free-standing COF nanofilms were transferred onto PAN substrates and silicon wafers to gain insight into their internal microstructure. Scanning electron microscopy (SEM) imaging reveals a uniform surface morphology for the TpPz nanofilm (Fig. 2g). Transmission electron microscopy (TEM) images demonstrate the regular structure of the TpPz nanofilm, while energy-dispersive X-ray spectroscopy (EDS) mapping confirms a uniform distribution of carbon, nitrogen, and oxygen elements (Fig. 2h). Additionally, atomic force microscopy (AFM) height profile measurements evince a thickness of 39.3 nm for the TpPz nanofilm (Fig. S4).

Morphology and structure of TpPz and Pd^0–TpPz composite membranes

A TpPz-based thin-film composite (TFC) membrane was fabricated on a Kevlar substrate *via* interfacial polymerization in a custom-built diffusion chamber (Fig. S1). This TpPz membrane was subsequently utilized to capture $PdCl_4^{2-}$ from simulated extrusion waste, followed by *in situ* growth of Pd nanoclusters to form a Pd^0–TpPz catalytic membrane (Fig. S2). Compared to the Kevlar substrate (Fig. S5), the TpPz composite membranes exhibited a C=C peak at 1578 cm^{-1}, consistent with the free-standing TpPz film. However, as exhibited in Fig. S6, the XRD diffraction peaks of the composite membranes align closely with those of the Kevlar substrate. This is because the signal from the relatively thin layer is masked by the intense background peaks of the Kevlar substrate.

The surface morphology of the as-fabricated membranes was examined using SEM images. Compared with the Kevlar substrate, the TpPz membranes demonstrated a more compact and uniform surface morphology without visible defects (Fig. S7a and S8a). AFM analysis further revealed a uniform TpPz surface with a low roughness (R_a = 15.0 nm, Fig. S7b and S8b). Cross-sectional TEM images distinctly depicted a 44.4 nm-thick nanofilm (Fig. S9a and S10a–b), consistent with the thickness observed for the freestanding film by AFM analysis. The well-defined boundaries and an even elemental distribution confirm the formation of a uniform COF nanofilm at the top surface of the Kevlar support (Fig. S10c).

Given the strong affinity of N-heterocyclic groups to Pd, TpPz membranes were explored for Pd capture. A noticeable color change from dark red to bright red for the TpPz surface confirmed Pd uptake from acidic leaching liquor. Leveraging the strong binding interaction between pyrazine groups and $PdCl_n^{X-}$, TpPz membranes with rich nanochannels were explored as templates for Pd nanocluster growth. *In situ* reduction with $NaBH_4$ yielded brown Pd^0–TpPz membranes with a uniform, low-roughness (21.2 nm, Fig. S8c and d) surface. Cross-sectional TEM images of the Pd^0–TpPz membranes revealed a 40.7 nm-thick film with highly dispersed nanoclusters (Fig. 2i). High-resolution TEM confirms the (111) crystal plane of the Pd nanoclusters with a crystal plane spacing of 0.225 nm (Fig. S9b). EDS mapping further confirmed their presence once again. These Pd nanoclusters evinced an average size of 1.96 nm in diameter with a narrow size distribution (Fig. 2j and S10d–e).

X-ray photoelectron spectroscopy (XPS) was used to determine the elemental composition and oxidation state of Pd within the TpPz membranes (Fig. 2k–l and S11–S13). XPS data revealed a Pd loading of 4.0% in the Pd^0–TpPz membrane (Table S1). Deconvolution of the C 1s, N 1s, and O 1s narrow scan spectra confirmed the successful formation of keto-enamine based TpPz (Fig. S12a–c). For Pd^0–TpPz membranes, the Pd 3d region displayed new characteristic peaks at 336.1 eV and 341.4 eV (Fig. 2k), corresponding to the $3d_{5/2}$ and $3d_{3/2}$ states of zero-valent Pd nanoclusters. However, weak peaks at 337.2 eV and 342.1 eV corresponding to the $3d_{5/2}$ and $3d_{3/2}$ states of Pd^{II} and PdO appeared, suggesting incomplete reduction and surface oxidation. This interpretation is further supported by the higher oxygen content observed in Pd^0–TpPz compared to TpPz. Thermogravimetric analysis (TGA) revealed high thermal stability for all membranes, with Pd^0–TpPz showing a higher residual weight (~15%) due to the presence of Pd (Fig. S14). Zeta potential measurements (Fig. S15) revealed the less electronegativity of the Pd^0–TpPz membrane, primarily due to the abundant nitrogen content and the presence of reduced Pd species. As shown in Fig. S16, the hydrogel substrate had the lowest WCA and the highest surface energy due to its high hydration and water content. As the TpPz layer formed on the Kevlar surface, the WCA gradually increased. In contrast,

the introduction of Pd nanoclusters increased the surface energy of the TpPz membranes, resulting in a lower WCA and a higher hydrophilicity for the Pd^0–TpPz membranes.

Adsorption performance of TpPz membranes

To capture trace concentrations of Pd ions from electroplating wastewater, the simulated Pd content was closely matched to those found in real-world processes. As exhibited in Fig. 3a, the TpPz membrane showed the highest removal efficiency for Pd^{2+} (>95.0%) among 17 competing metal ions tested. In addition, the TpPz membrane with a 24-hour reaction time exhibited the highest adsorption efficiency for Pd^{2+} (Fig. S17), mainly because of the thickening of the TpPz selective layer on the Kevlar substrate as a function of reaction time. SEM images of TpPz membranes at different reaction times corroborated this observation, revealing particle formation on the membrane surface on prolonging the reaction time (Fig. S18). When the TpPz selective layer was fabricated using different porous substrates (Kevlar, PAN, PES, and PS), the highest removal efficiency of 95.6% for Pd was achieved using the TpPz–Kevlar composite membrane (Fig. 3b). The Kevlar substrate, a poly(*p*-phenylene terephthalamide) hydrogel, possesses abundant aromatic amino ($-NH_2$) and carbonyl (C=O) functional groups. These groups create strong molecular complementarity with the TpPz COF through enhanced π–π stacking interactions and hydrogen bonding networks. This compatibility enables the formation of an exceptionally uniform COF layer with a well-defined thickness of 40.0 nm. In contrast, Kevlar substrates without the TpPz layer showed minimal Pd^{2+} removal (<5%), highlighting the TpPz membrane's superior capture performance (Fig. 3c). Adsorption kinetics of TpPz membranes

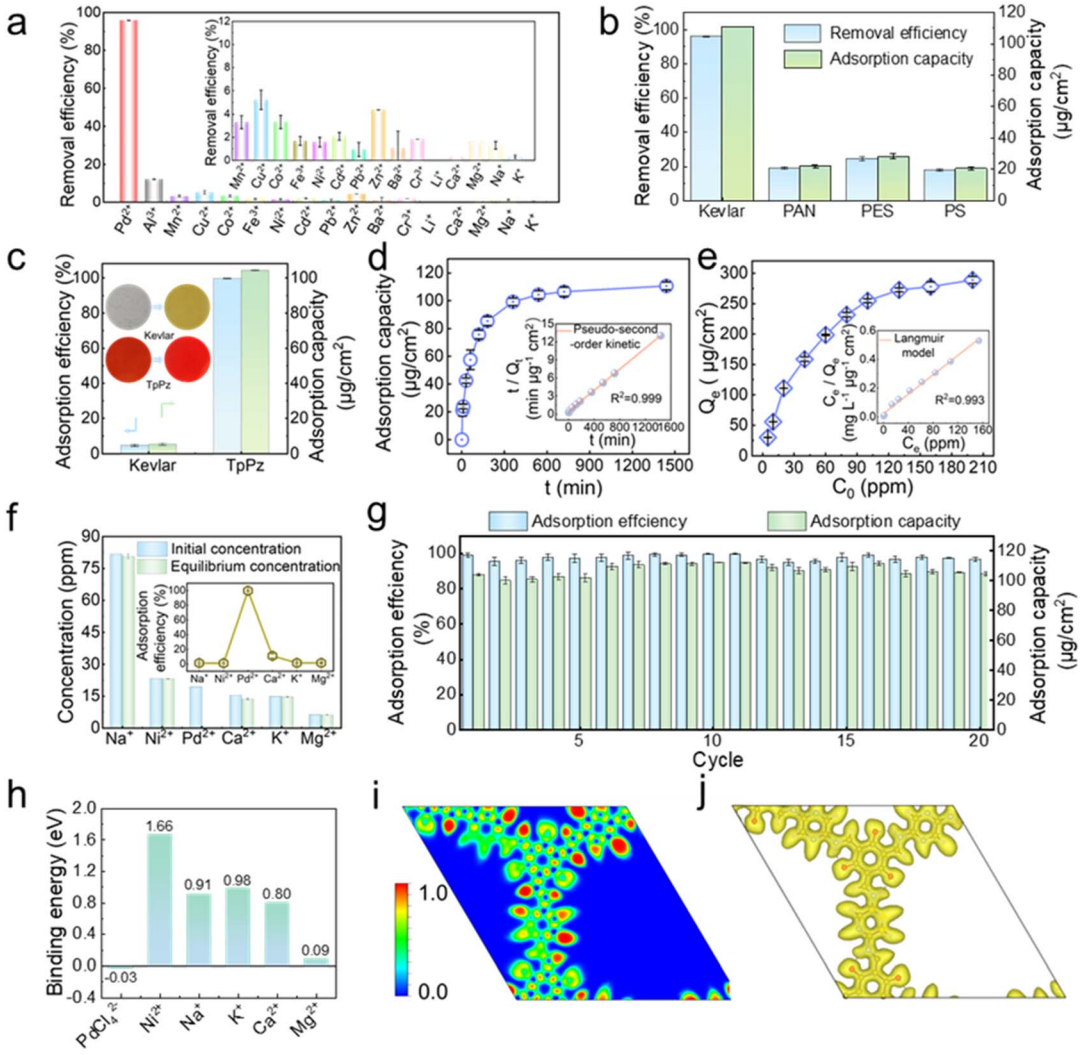

Fig. 3 Capture performance of TpPz membranes. (a) The selectivity of TpPz membranes towards metal ions; (b) the removal efficiency of Pd^{2+} with different substrates; (c) comparison of Pd^{2+} removal performance between the Kevlar substrate and TpPz; (d) adsorption kinetics of Pd^{2+} on TpPz membranes; (e) adsorption isotherm of Pd^{2+} on TpPz membranes; (f) adsorption capacity of TpPz membranes in simulated leaching liquor; (g) the Pd^{2+} adsorption efficiency (left axis) and adsorption capacity (right axis) of TpPz in twenty successive adsorption–desorption cycles; (h) the adsorption energy between six metal ions and TpPz obtained using density functional theory (DFT) calculations; (i) projection of the 3D ELF distribution of TpPz onto the COF plane; (j) 3D ELF distribution of TpPz COF.

demonstrated rapid $PdCl_4^{2-}$ uptake, reaching equilibrium within 12 hours (Fig. 3d). The exceptionally high correlation coefficient ($R^2 = 0.9999$) for the pseudo-second-order kinetic plot, in contrast to the lower R^2 (0.9559) for the pseudo-first-order plot, indicates that the Pd^{2+} adsorption on TpPz membranes is predominantly driven by a chemical process (Fig. S19). The TpPz membrane exhibited a steep adsorption profile for Pd^{2+}, signifying a strong affinity for Pd^{2+}. The Langmuir model ($R^2 = 0.993$) provided a better fit to the equilibrium adsorption data than the Freundlich model ($R^2 = 0.975$), as indicated by the comparison of correlation coefficients (Fig. 3e, S20 and Table S2).

As the predominant palladium species at pH 2.5 are $PdCl_3^-$ or $PdCl_4^{2-}$, these anionic species are effectively adsorbed onto the TpPz membrane surface through strong local electrostatic interactions. Fig. S21a illustrates the impact of feed pH on Pd adsorption. A substantial increase in Pd adsorption capacity was observed as pH rose from 1.0 to 3.0. This enhancement stems from the competitive adsorption between excessive chloride ions and protonated sites for $PdCl_4^{2-}$ at lower pH levels. When the pH exceeded 3, the precipitation of palladium as $Pd(OH)^+/Pd(OH)_2$ may compromise the accurate determination of adsorption capacity.[41] Furthermore, a slight increase in the adsorption capacity, from 100.3 to 113.6 μg cm^{-2}, was observed as the temperature increased from 15 °C to 45 °C, suggesting the endothermic nature of the palladium adsorption process (Fig. S22b). Notably, the TpPz membrane exhibited remarkable selectivity for $PdCl_4^{2-}$, even in the presence of competitive ions including Na^+, K^+, Ca^{2+}, Mg^{2+}, and Ni^{2+} (Fig. 3f). Following palladium elution with thiourea, the bright red Pd(II)-saturated TpPz membrane reverted to its original dark red color (Fig. S22). Over twenty adsorption–desorption cycles, the membrane exhibited minimal loss in adsorption capacity and efficiency, indicating its excellent recyclability (Fig. 3g).

Compared to the pristine TpPz membranes, the peak at 3259 cm^{-1} (pyrazine N) in Pd^0–TpPz is significantly diminished, likely due to coordination between pyrazine N and palladium, which weakens the original pyrazine N absorption peak (SI, Fig. S23). In N 1s spectra of TpPz (Fig. S12b), two binding energy peaks at 399.3 and 398.4 eV are attributed to pyrazine N and C–NH, respectively. After *in situ* reduction treatment, the N 1s spectrum of Pd^0–TpPz shows that these peaks shift to higher binding energies by 1.33 eV and 1.62 eV, respectively (Fig. S13b). The O 1s peaks in the Pd^0–TpPz membrane (Fig. S12c and S13c) also shift to higher binding energies by 1.61 eV and 1.48 eV. These changes indicate that the Pd adsorption onto TpPz is a chemical process, where both pyrazine-N and ketone groups in TpPz are coordinated with Pd^{II}. Fluorescence imaging reveals red fluorescence of the TpPz nanofilm, attributed to its highly conjugated structure. An obvious decline in fluorescence intensity of palladium-absorbed TpPz suggests its strong affinity for palladium (Fig. S24), resulting in fluorescence quenching.[42] Electronic localization function (ELF) contour maps (Fig. 3i and j) reveal a higher localized charge density at the pyrazine-N site compared to the oxygen atoms in the TpPz skeleton. Analysis of the electronic structure suggests limited lone pair delocalization at pyrazine-N atoms, resulting in stronger electron donation from these nitrogen centers.[43] This enhanced electron-donating ability of the pyrazine-N site contributes to selective palladium adsorption. Furthermore, the electrostatic surface potential of TpPz (Fig. S25) indicates the presence of abundant positive and weak negative charges around the N atom, further facilitating palladium capture. Density functional theory (DFT) calculations were performed to determine the adsorption potential energies of various metal ions on the rational N sites (Fig. 3h and S26). The binding energy (E_{ads}) between $PdCl_4^{2-}$ and TpPz was calculated to be −0.03 eV, indicating a strong Pd affinity. In contrast, the positive ΔE_{ads} values for the other metals revealed the repulsive force against TpPz, primarily attributed to electrostatic interactions between the cations and the positively charged pyrazine and secondary amine groups under acidic conditions.[44]

Separation and catalytic performance of Pd^0–TpPz membranes

To evaluate the separation performance of TpPz membranes, methyl blue (MB) was employed as the model pollutant. As the Tp concentration increased from 0.5 mM to 1.0 mM, water permeability of the TpPz membrane decreased from 182 LMH/bar to 54 LMH/bar, while the MB rejection rate increased from 88.8% to 96.3% (Fig. S27). SEM images revealed the formation of particle deposits on the membrane surface at higher Tp concentrations (Fig. S28). Moreover, the WCA of the TpPz membrane increased with an increasing Tp concentration, suggesting a reduced surface hydrophilicity. This trend is attributed to the accumulated Tp building blocks with a hydrophobic structure (Fig. S29). The impact of palladium adsorption duration on the catalytic and separation performance of Pd^0–TpPz membranes was further explored. The Pd loading increased with longer adsorption time, but this had a negligible effect on their water flux (Fig. S30). As depicted in Fig. 4a, insufficient adsorption time results in low palladium loading on the TpPz membrane, leading to weak catalytic activity for Cr^{VI} and RhB. Conversely, excessive adsorption time would cause the aggregation of Pd nanoclusters during reduction (Fig. S31). An optimal adsorption time of 1 hour was determined to balance catalytic activity and separation performance while minimizing the aggregation. The Pd^0–TpPz membrane was evaluated for organic dye separation. At a flux of 85.4 L m^{-2} h^{-1} bar^{-1}, the rejections for Evans blue (EB), Direct Red 23 (DR23), Eriochrome black T (EBT), Congo red (CR), and methyl blue (MB) were high, ranging from 93.4% to 99.8%. However, these loose-structured membranes exhibited much lower removal efficiency for smaller organic molecules like rhodamine B (RhB), orange II, methyl orange (MO), 4-nitroaniline (4-NA), 4-nitrophenol (4-NP), and Cr^{VI}, with the low rejections from 1.5% to 41.2% (Fig. 4b, UV spectra in SI, Fig. S32). In this context, we further evaluated the catalytic performance of Pd^0–TpPz using Cr^{VI} and RhB as model pollutants. With constant Cr^{VI} (0.2 mM) and RhB (50 mg L^{-1}) concentrations, the usage of 75 mmol formic acid led to a 98.6% Cr^{VI} conversion rate, while using 6 mmol $NaBH_4$ resulted in a 98.8% RhB conversion rate (Fig. S33 and S34). As a control, the TpPz

membrane alone, when used with the reducing agent, exhibited minimal catalytic activity, as indicated by a slight decrease in the absorption peak after 20 minutes. In contrast, introducing the Pd^0–TpPz membrane coupon (~4.9 cm^2) resulted in a significant reduction in the RhB or Cr^{VI} characteristic peak (Fig. S35). We further demonstrated their superior catalytic activity for a broader range of pollutants (*e.g.*, 97.9% for orange II, 98.7% for MO, 98.6% for 4-NP, and 99.1% for 4-NA) (Fig. 4c and S36).

Pd^0–TpPz membranes demonstrated exceptional catalytic activity for both Cr^{VI} and RhB reductions under static conditions (Fig. 4d and S37). Complete reduction of Cr^{VI} was achieved within 30 min, while RhB reduction required 60 min. Both processes followed first-order kinetics, with calculated K_{cat} values of 6.75×10^{-2} min^{-1} for Cr^{VI} and 6.15×10^{-2} min^{-1} for RhB, respectively (Fig. S38a and S39). These values are an order of magnitude higher than those reported for other catalytic membranes under similar conditions.[45] Despite their excellent catalytic activity under static conditions, the limited contact with reactants/reductants hinders their suitability for continuous industrial water treatment. However, the uniform, defect-free surface and evenly distributed Pd nanoclusters within the COF layer position the Pd^0–TpPz membrane as a promising candidate for superior performance in continuous flow catalytic reactions. Notably, the Pd^0–TpPz membrane exhibited exceptional performance in both water permeation and dynamic catalysis. When applied at 4.0 bar, Pd^0–TpPz demonstrated an excellent water permeability of 85.4 L m^{-2} h^{-1} bar^{-1} and a remarkably high conversion rate of 98.6% for Cr^{VI} and 98.8% for RhB. Moreover, Cr^{VI} and RhB conversion rates remained above 95% even at an elevated pressure of 7 bar (Fig. S39b and 4e). The ultrathin TpPz nanofilm, with rich evenly dispersed and ultrafine Pd nanoclusters, facilitated rapid mass transfer and reaction kinetics. The apparent rate constants, K_{cat}, for Cr^{VI} and RhB were determined to be 4.99 ms^{-1} and 5.46 ms^{-1}, respectively (Fig. S39c and 4f). These values are significantly higher than those observed in static catalysis (6.75×10^{-2} min^{-1} and 6.15×10^{-2} min^{-1}), highlighting the advantages of dynamic catalysis. By rapidly removing products, dynamic catalysis can overcome thermodynamic limitations and enhance catalytic efficiency.[46] Moreover, the Pd^0–TpPz membrane exhibits exceptional pH tolerance, maintaining over 99% catalytic efficiency for 10 cycles in both strongly alkaline (0.03 M $NaBH_4$, pH 12) and acidic (0.4 M formic acid, pH 2)

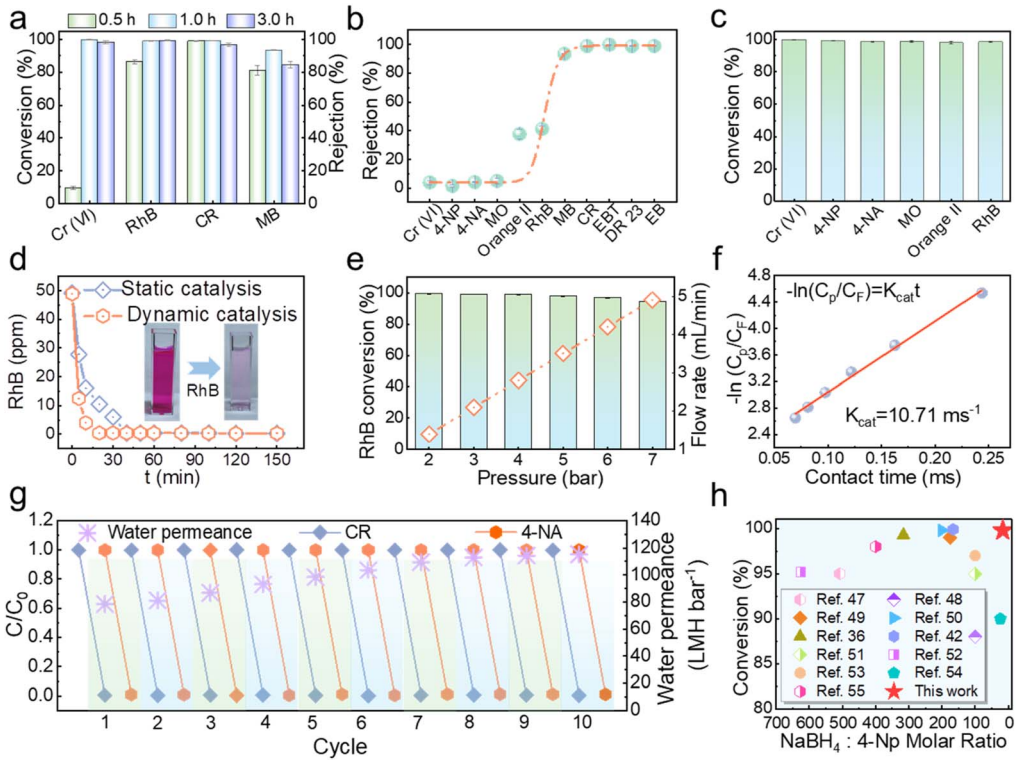

Fig. 4 Separation and catalytic performance of Pd^0–TpPz membranes. (a) Separation and catalytic performance of Pd^0–TpPz membranes prepared with different Pd^{2+} adsorption times. (b) Separation performance of Pd^0–TpPz membranes for different dyes; (c) catalytic conversion performance of Pd^0–TpPz membranes for small molecule pollutants; (d) comparison of dynamic and static catalytic properties of Pd^0–TpPz membranes for RhB; (e) RhB conversion and feed flow rate under different pressures; (f) plot of $-\ln(C_P/C_F)$ *versus* Pd^0–TpPz membrane contact time for the dynamic catalysis of RhB, showing first-order kinetics; (g) separation catalytic cycle experiments of Pd^0–TpPz membranes for CR and 4-NA mixtures; (h) performance comparison of the Pd^0–TpPz membranes with other reported materials. Cu/Cu_2O network CMMR;[47] Cu–Ag PES CMMR;[48] AuNPs PVDF CMMR;[49] Ag/ZIF-8 CMMR;[50] Nano Cu/ZIF-8 CMMR;[36] Pd-TpBpy CMMR;[42] PNG/Ag CMMR;[51] BNPC-1000 nanoparticles;[52] Co@NG-900 nanoparticles;[53] 0.2 wt% Pd/TiO_2 nanoparticles;[54] $Cu_{1.5}$-FCLL nanoparticles.[55]

environments. This demonstrated stability across extreme pH ranges (2–12) confirms its suitability for real wastewater treatment. Pd–TpPz membranes exhibited minimal Pd leaching (~8.0 ppb, 0.015%) over 96 h (Fig. S40), confirming their outstanding structural stability.

To address the challenges posed by real-world wastewater, we assessed the water decontamination efficiency of Pd^0–TpPz membranes using a mixture of CR and Cr^{VI} as feed. The membrane demonstrated impressive efficiency in sieving CR while simultaneously catalyzing the reduction of Cr^{VI}. Superior performance was also achieved for treating a mixture of 4-NA and CR (Fig. S41 and S42). The cyclic regeneration ability of the membrane was evaluated through ten consecutive cycles of operation with mixed wastewaters containing CR, Cr^{VI} or 4-NA. Remarkably, the removal rates remained consistently above 99.0% (Fig. 4g and S43). For the 4-NA and CR mixture, the water flux increased from 78.5 to 115.3 L m^{-2} h^{-1} bar^{-1}, likely stemming from the swelling of the Kevlar substrate under alkaline conditions. In contrast, for the Cr^{VI} and CR mixture, the water flux decreased from 79.0 to 45.8 L m^{-2} h^{-1} bar^{-1}, potentially caused by pore blockage from metal complexes. After ten catalytic cycles, a slight increase in Pd nanoparticles was observed on the surface of the Pd^0–TpPz membrane (Fig. S44), likely due to the reduction of residual Pd^{II} during the catalytic process. These results highlight the robust stability of the Pd^0–TpPz membrane, with both catalytic performance and structural integrity remaining intact under prolonged testing. Fig. S45 depicts that the MWCO of the Pd^0–TpPz membrane was determined to be 35 kDa. In comparison to the pore size of 1.8 nm measured through N_2 adsorption, the Stokes diameter of Pd^0–TpPz significantly increased to 4.2 nm. This pore expansion is closely related to the reduction process, where interactions with methanol and bubble formation caused partial swelling of the Kevlar substrate. As a result, the weakened interaction between the Pd–COF layer and the Kevlar substrate led to a substantial increase in membrane pore size. The Pd^0–TpPz membrane demonstrated superior catalytic performance for 4-NP reduction, even at low $NaBH_4$ ratios, compared to other reported materials (Fig. 4h).

The Kevlar substrate and TpPz membranes, lacking antibacterial components, exhibited minimal antibacterial activity against Gram-negative *Escherichia coli* (*E. coli*) (Fig. S46). In contrast, Pd^0–TpPz membranes demonstrated remarkably high antibacterial properties, achieving a 98.1% bacteriostasis rate (BR) as measured by the plate-counting method. This high efficacy stems from the generation of intracellular reactive

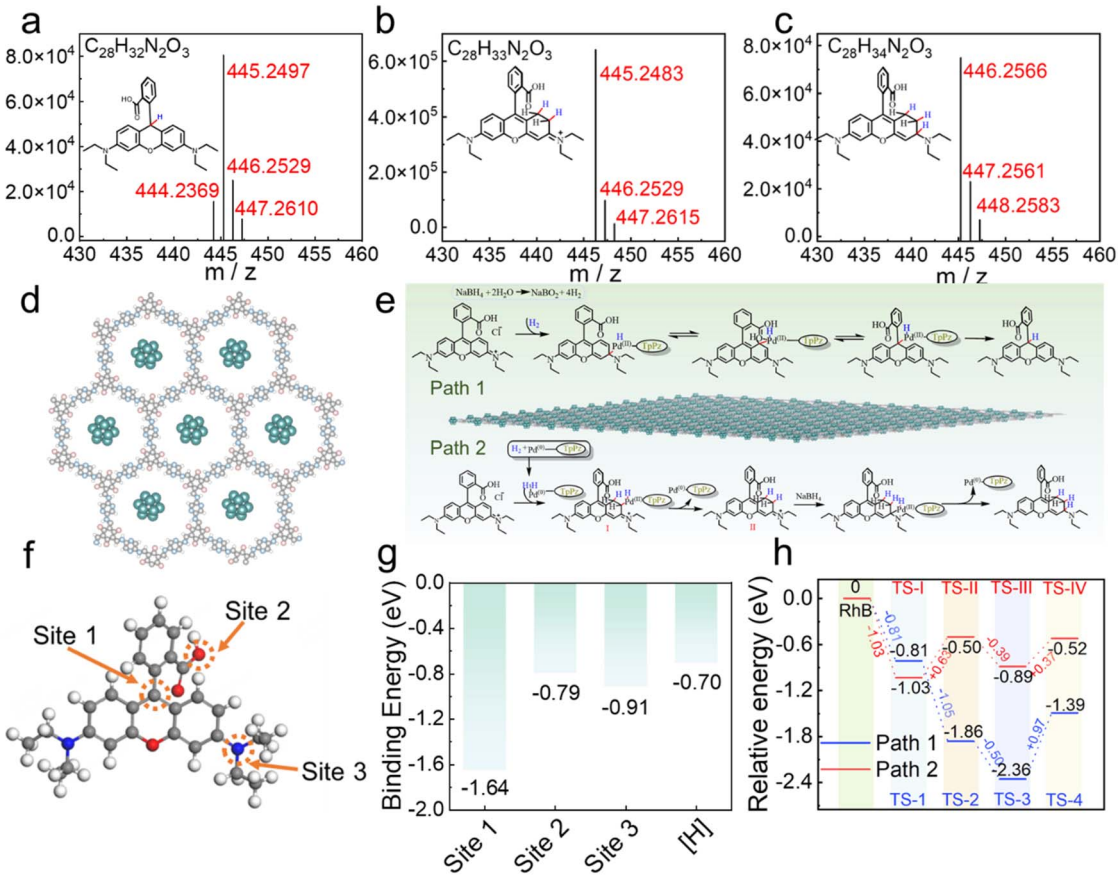

Fig. 5 Investigation of the catalytic mechanism in Pd^0–TpPz membranes. (a–c) LC-MS spectra of the three main products after RhB reduction; (d) composite structure of TpPz and Pd nanoclusters; (e) schematic diagram of the mechanism of the two reduction pathways of RhB; (f) schematic diagram of three different sites of RhB; (g) adsorption energy between Pd^0–TpPz with different sites of RhB or activities of H; (h) the relative energy of intermediates in different reduction pathways of RhB.

oxygen species (ROS) induced by the Pd nanoclusters, leading to bacterial inactivation.

Theoretical calculations

To investigate RhB degradation pathways in the Pd^0–TpPz/$NaBH_4$ system, LC-MS analyses identified three potential final products resulting from hydrogenation, tautomerization, and reduction (Fig. 5a–c and S47). Based on these products and reaction sites of RhB molecules, two degradation pathways were proposed (Fig. 5d–e and S48). To elucidate the $NaBH_4$ reduction mechanism, DFT calculations were conducted on a composite structure of TpPz COF and Pd nanoclusters. On comparing adsorption energies, Pd^0–TpPz preferentially adsorbs RhB over active H (Fig. 5f–g). DFT calculations of intermediate energies along the proposed pathways suggest that while the surface of Pd nanoclusters may adsorb a significant amount of active H, the generation of H is thermodynamically favorable, as indicated by a previous calculation of −0.70 eV adsorption energy between Pd^0–TpPz and H.[56,57]

DFT calculations reveal that the rate-limiting step in pathway 1 is the hydrogenation from ST-3 to ST-4, with an energy barrier of 0.87 eV (Fig. 5h). In pathway 2, the rate-limiting step for generating product II is the hydrogenation from ST-I to ST-II (0.53 eV). For product IV, the rate-limiting step is the hydrogenation from ST-III to ST-IV (0.37 eV). Lower energy barriers favor the formation of ST-II and ST-IV. Once ST-II forms, its subsequent conversion to ST-III is thermodynamically favorable. In addition, the energy barrier for the transition from ST-III to ST-IV is lower than that from ST-I to ST-II. From an overall reaction perspective, the formation of ST-IV from ST-II is energetically downhill. Thus, we anticipate a higher yield of ST-IV compared to ST-II. However, since ST-II is an intermediate in the formation of ST-IV, it is expected to be present in the final mixture. While the rate-limiting step for the formation of ST-4 has a higher energy barrier than those for ST-II and ST-IV, the overall barrier is still relatively low (less than 1.0 eV), suggesting that ST-4 may also be present in the final mixture.[58] These DFT calculation results align well with the findings from the LC-MS analysis.

Experimental

Fabrication of TpPz membranes

TpPz membranes were fabricated using interfacial polymerization (IP) between Tp and Pz in a lab-made diffusion chamber with an effective area of 16.6 cm^2 (Fig. S1). Firstly, the as-fabricated Kevlar substrate was surface dried using an air knife and subsequently fixed at this module. Secondly, an aqueous phase with different Pz concentrations was added to the cell facing the backside of the Kevlar substrate, and a dichloromethane phase with different Tp concentrations was introduced to another cell. The IP at the membrane surface was maintained at room temperature and under static conditions for different reaction times. Afterward, the obtained thin-film composite (TFC) membranes were rinsed and stored in deionized water before use.

Capture of divalent palladium ions in TpPz membranes

Prior to the adsorption experiment, a Pd^{2+} stock solution (20 ppm) was prepared using Na_2PdCl_4, with the solution pH adjusted to 2.5 using hydrochloric acid. A piece of the TpPz membrane (3 × 3 cm^2) was immersed in a 50 mL Pd^{2+} stock solution. Subsequently, the solution was placed in a thermostatic shaker with a speed of 170 rpm at room temperature. The residual Pd^{2+} content was recorded at different time intervals using ICP-OES (Shimadzu, shimao2u, Japan). The Pd-saturated membrane was denoted as Pd^{2+}–TpPz (Fig. S2). More specific details on the Pd adsorption using TpPz membranes can be found in the SI.

Fabrication of Pd^0–TpPz membranes

In situ reduction of Pd ions on the TpPz membrane was performed to fabricate nanoconfined catalytic COF membranes. In a typical procedure, a piece of the Pd^{2+}–TpPz membrane (3 × 3 cm^2) was placed in a 20 mM $NaBH_4$ solution (50 mL, $V_{methanol}$: V_{water} = 1 : 9) for *in situ* growth of Pd nanoclusters. After 10 min of reduction, the resulting catalytic membranes (termed Pd^0–TpPz) were rinsed and stored in DI water before use (Fig. S2).

Separation-coupled catalytic performance of Pd^0–TpPz membranes

A simulated mixed solution containing 100 ppm CR and 50 ppm 4-NA was prepared as feed. The Pd^0–TpPz membrane was placed in a dead-end cell with an effective surface area of 4.90 cm^2. A 150 mL aqueous feed solution containing 6 mM $NaBH_4$ was filtered through a Pd^0–TpPz membrane under 4 bar. The permeate was collected and analyzed for 4-NA concentration using UV-vis spectroscopy. All experiments were conducted in triplicate. For the reduction of the Cr^{6+}/CR mixed system, FA (75 mmol) was used as the reducing agent, while other procedures remained identical to those used for 4-NA/CR. Specific details on the independent rejection and catalytic conversion experiments can be found in the SI.

Conclusions

In this work, we introduce a dual-function system for rapid and efficient water purification: molecular separation and nanoconfined catalytic conversion. This system is achieved by impregnating COF membranes with *in situ* recycled Pd nanoclusters (Pd, ~1.96 nm). Calculations of the ELF and adsorption energy confirmed the robust affinity between pyrazine COF and Pd^{II}. The resulting Pd^0–TpPz membrane exhibited exceptional performance in both molecular separation of large dye molecules (*e.g.*, CR, EBT, and DR23) and catalytic reduction of toxic molecules and high-valence metals (*e.g.*, RhB, 4-NA, and Cr^{VI}). Importantly, at low reducing doses, the dynamic catalytic K_{cat} for Cr^{VI} and RhB are as high as 4.99 ms^{-1} (2.99 × 10^5 min^{-1}) and 5.46 ms^{-1} (3.28 × 10^5 min^{-1}), respectively, highlighting the high efficiency of dynamic catalysis. This one-step process offers a significant advantage over conventional intensive and multi-step water treatment techniques. Molecular calculations and experimental analyses revealed that RhB degradation using

Pd^0–TpPz proceeds *via* a hydrogenation reduction mechanism. Furthermore, this membrane demonstrated excellent recyclability and antimicrobial activity, making it a promising candidate for practical water treatment applications. This dual-function system has the potential to be extended to various COF adsorptive membranes and applied to the purification of complex, nontraditional water sources.

Author contributions

Guishan Hu: data curation, investigation, validation, writing – original draft. Binyu Zhou and Yu Zhen: data curation, investigation. Junyong Zhu, Yatao Zhang and Yong Wang: funding acquisition, conceptualization, resources, project administration, writing – review & editing, supervision. Jingwei Hou and Bart Van der Bruggen: supervision, writing – review & editing.

Conflicts of interest

The authors declare that they have no known competing financial interests or personal relationships that could have appeared to influence the work reported in this paper.

Data availability

Detailed experimental and computational data are provided in the SI. This includes materials and chemicals, membrane fabrication procedures, adsorption performance studies (isotherms, kinetics, cycling tests), catalytic evaluation under batch and continuous-flow conditions, membrane characterization (morphology, pore structure, stability), theoretical calculations, and all relevant analytical data. All raw and processed data supporting these findings are available in the SI in tabulated or graphical form. Data files include spectral analyses, kinetic fittings, microscopy images, and computational result. See DOI: **https://doi.org/10.1039/d5sc04204f**.

Acknowledgements

This work was supported by the National Key Research and Development Program of China (2024YFB3815400), the Science and Technology Innovation Leading Talent Support Program of Henan Province (254200510023), and the Outstanding Youth Fund of Henan Scientific Committee (252300421182). The characterization and simulations were performed at the Center of Advanced Analysis & Computational Science at Zhengzhou University and the National Supercomputing Center in Zhengzhou, respectively.

Notes and references

1 B. C. Hodges, E. L. Cates and J.-H. Kim, *Nat. Nanotechnol.*, 2018, **13**, 642–650.
2 J. R. Werber, C. O. Osuji and M. Elimelech, *Nat. Rev. Mater.*, 2016, **1**, 16018.
3 H. Quon and S. Jiang, *npj Clean Water*, 2023, **6**, 56.
4 Y. Zhang, J. Huo and X. Zheng, *Science*, 2021, **374**, 1332.
5 L. F. Petrik, H. H. Ngo, S. Varjani, P. Osseweijer, D. Xevgenos, M. van Loosdrecht, M. Smol, X. Yang and J. Mateo-Sagasta, *One Earth*, 2022, **5**, 122–125.
6 A. Christou, V. G. Beretsou, I. C. Iakovides, P. Karaolia, C. Michael, T. Benmarhnia, B. Chefetz, E. Donner, B. M. Gawlik, Y. Lee, T. T. Lim, L. Lundy, R. Maffettone, L. Rizzo, E. Topp and D. Fatta-Kassinos, *Nat. Rev. Earth Environ.*, 2024, **5**, 504–521.
7 S. Xu, X. Mi, P. Wang, Y. Mao, Q. Zhou and S. Zhan, *Adv. Funct. Mater.*, 2023, **33**, 2308204.
8 M. Gil-Sepulcre and A. Llobet, *Nat. Catal.*, 2022, **5**, 79–82.
9 B. Van der Bruggen, *Nat. Rev. Chem.*, 2021, **5**, 217–218.
10 J. Zhang, B. Liu, L. Cai, Y. Li, Y. Zhang, M. Liu, L. Jia, S. Fan, L. Lei, M. Zhu, X. Zhu, X. Ke, A. Huang, H. Jiang and R. Chen, *Adv. Membr.*, 2023, **33**, 100070.
11 J. Pan and F. J. M. Xia, *Matter*, 2022, **5**, 2526–2528.
12 G. Pacchioni, *Nat. Rev. Mater.*, 2017, **2**, 17025.
13 H. Peng, S. K. Lau and W. Yong, *Adv. Membr.*, 2024, **4**, 4100093.
14 S. Zhang, L. Shen, H. Deng, Q. Liu, X. You, J. Yuan, Z. Jiang and S. J. A. m. Zhang, *Adv. Mater.*, 2022, **34**, 2108457.
15 Y. Kang, Y. Wang, H. Zhang, Z. Wang, X. Zhang and H. Wang, *Chem. Soc. Rev.*, 2024, **53**, 7939.
16 J. Li, H. Peng, K. Liu and Q. Zhao, *Adv. Mater.*, 2024, **36**, 2309406.
17 P. Shao, R. Yao, G. Li, M. Zhang, S. Yuan, X. Wang, Y. Zhu, X. Zhang, L. Zhang, X. Feng and B. Wang, *Angew. Chem., Int. Ed.*, 2020, **59**, 4401–4405.
18 T. Liu, Y. Zhang, Z. Shan, M. Wu, B. Li, H. Sun, G. Su, R. Wang and G. Zhang, *Nat. Water*, 2023, **1**, 1059–1067.
19 J. Huang, Y. Zhang, J. Guo, F. Yang, J. Ma, Y. Bai, L. Shao, S. Liu and H. Wang, *Nat. Sustain.*, 2024, **7**, 901–909.
20 H. B. Park, J. Kamcev, L. M. Robeson, M. Elimelech and B. D. Freeman, *Science*, 2017, **356**, eaab0530.
21 X. Lu and M. Elimelech, *Chem. Soc. Rev.*, 2021, **50**, 6290–6307.
22 M. F. Jimenez-Solomon, Q. Song, K. E. Jelfs, M. Munoz-Ibanez and A. G. Livingston, *Nat. Mater.*, 2016, **15**, 760–767.
23 X. Zhang, Y. Li, C. Van Goethem, K. Wan, W. Zhang, J. Luo, I. F. J. Vankelecom and J. Fransaer, *Matter*, 2019, **1**, 1285–1292.
24 M. Matsumoto, L. Valentino, G. M. Stiehl, H. B. Balch, A. R. Corcos, F. Wang, D. C. Ralph, B. J. Mariñas and W. R. Dichtel, *Chem*, 2018, **4**, 308–317.
25 P. Y. Qian, A. Cheng, R. Wang and R. Zhang, *Nat. Rev. Microbiol.*, 2022, **20**, 671–684.
26 K. T. Tan, S. Ghosh, Z. Wang, F. Wen, D. Rodríguez-San-Miguel, J. Feng, N. Huang, W. Wang, F. Zamora, X. Feng, A. Thomas and D. Jiang, *Nat. Rev. Methods Primers*, 2023, **3**, 1.
27 F. Auras, L. Ascherl, V. Bon, S. M. Vornholt, S. Krause, M. Döblinger, D. Bessinger, S. Reuter, K. W. Chapman, S. Kaskel, R. H. Friend and T. Bein, *Nat. Chem.*, 2024, **16**, 1373–1380.
28 Z. Wang, S. Zhang, Y. Chen, Z. Zhang and S. Ma, Covalent organic frameworks for separation applications, *Chem. Soc. Rev.*, 2020, **49**, 708–735.

29 S. Yuan, X. Li, J. Zhu, G. Zhang, P. Van Puyvelde and B. Van der Bruggen, Covalent organic frameworks for membrane separation, *Chem. Soc. Rev.*, 2019, **48**, 2665–2681.
30 F. Meng, S. Bi, Z. Sun, D. Wu and F. Zhang, *Angew. Chem., Int. Ed.*, 2022, **61**, e202210447.
31 L. Zheng, Z. Zhang, Z. Lai, S. Yin, W. Xian, Q.-W. Meng, Z. Dai, Y. Xiong, X. Meng, S. Ma, F.-S. Xiao and Q. Sun, *Nat. Commun.*, 2024, **15**, 6837.
32 W. Zhao, Q. Zhu, X. Wu and D. Zhao, *Chem. Soc. Rev.*, 2024, **53**, 7531–7565.
33 W. Xian, D. Wu, Z. Lai, S. Wang and Q. Sun, *Acc. Chem. Res.*, 2024, **57**, 1973–1984.
34 H. Yang, J. Xu, H. Cao, J. Wu and D. Zhao, *Nat. Commun.*, 2023, **14**, 2726.
35 Y. Li, L. Shen, D. Zhao, J. Teng, C. Chen, Q. Zeng, S. Raza, H. Lin and Z. Jiang, *Coord. Chem. Rev.*, 2024, **514**, 215873.
36 Y. Zhang, H. Wang, W. Wang, Z. Zhou, J. Huang, F. Yang, Y. Bai, P. Sun, J. Ma, L. E. Peng, C. Y. Tang and L. Shao, *Matter*, 2024, **7**, 1406–1439.
37 B. Hosseini Monjezi, K. Kutonova, M. Tsotsalas, S. Henke and A. Knebel, *Angew. Chem., Int. Ed.*, 2021, **60**, 15153–15164.
38 I. Favier, D. Pla and M. Gómez, *Chem. Rev.*, 2020, **120**, 1146–1183.
39 Q. Liao, Q. Sun, H. Xu, Y. Wang, Y. Xu, Z. Li, J. Hu, D. Wang, H. Li and K. Xi, *Angew. Chem., Int. Ed.*, 2023, **62**, e202310556.
40 M. Fan, W. D. Wang, Y. Zhu, X. Sun, F. Zhang and Z. Dong, *Appl. Catal., B*, 2019, **257**, 117942.
41 Y. Ho Kim and Y. Nakano, Adsorption mechanism of palladium by redox within condensed-tannin gel, *Water Res.*, 2005, **39**, 1324–1330.
42 A. L. Garner, F. Song and K. Koide, *J. Am. Chem. Soc.*, 2009, **131**, 5163–5171.
43 X. Liu, F. Gao, T. Jin, K. Ma, H. Shi, M. Wang, Y. Gao, W. Xue, J. Zhao, S. Xiao, Y. Ouyang and G. Ye, *Nat. Commun.*, 2023, **14**, 5097.
44 S. Cao, D. Li, A. A. Uliana, Y. Jiang, J. Zhu, Y. Zhang and B. Van der Bruggen, *Appl. Catal., B*, 2023, **323**, 122175.
45 R. Xie, F. Luo, L. Zhang, S.-F. Guo, Z. Liu, X.-J. Ju, W. Wang and L.-Y. Chu, *Small*, 2018, **14**, 1703650.
46 Y. Zhong, T. Li, H. Lin, L. Zhang, Z. Xiong, Q. Fang, G. Zhang and F. Liu, *Chem. Eng. J.*, 2018, **344**, 299–310.
47 C. Meng, B. Ding, S. Zhang, L. Cui, K. K. Ostrikov, Z. Huang, B. Yang, J.-H. Kim and Z. Zhang, *Nat. Commun.*, 2022, **13**, 4010.
48 X.-J. Bai, D. Chen, Y.-N. Li, X.-M. Yang, M.-Y. Zhang, T.-Q. Wang, X.-M. Zhang, L.-Y. Zhang, Y. Fu, X. Qi and W. Qi, *J. Membr. Sci.*, 2019, **582**, 30–36.
49 Y. Chen, S. Fan, B. Qiu, J. Chen, Z. Mai, Y. Wang, K. Bai and Z. Xiao, *ACS Appl. Mater. Interfaces*, 2021, **13**, 24795–24803.
50 J. Wang, Z. Wu, T. Li, J. Ye, L. Shen, Z. She and F. Liu, *Chem. Eng. J.*, 2018, **334**, 579–586.
51 K. G. N. Quiton, M.-C. Lu and Y.-H. Huang, *Chemosphere*, 2021, **262**, 128371.
52 Z. Hasan, D.-W. Cho, C.-M. Chon, K. Yoon and H. Song, *Chem. Eng. J.*, 2016, **298**, 183–190.
53 W. Liu, S.-Q. Li, W.-X. Liu, Q. Zhang, J. Shao and J.-L. Tian, *J. Environ. Chem. Eng.*, 2021, **9**, 105689.
54 L. Xing, H. Gao, X. Chen, D. Jia, X. Huang and M. Yang, *Chem. Eng. Sci.*, 2020, **217**, 115525.
55 X. Huang, C. Lin, X. Ding, Y. Yang and H. Ge, *Mater. Sci. Eng., B*, 2023, **293**, 116465.
56 P. Makvandi, C.-y. Wang, E. N. Zare, A. Borzacchiello, L.-n. Niu and F. R. Tay, *Adv. Funct. Mater.*, 2020, **30**, 1910021.
57 B. Jiang, M. Gil-Sepulcre, P. Garrido-Barros, C. Gimbert-Suriñach, J.-W. Wang, J. Garcia-Anton, P. Nolis, J. Benet-Buchholz, N. Romero, X. Sala and A. Llobet, *Angew. Chem., Int. Ed.*, 2022, **61**, e202209075.
58 J. Lu, W. Mu, C. Qin, T. Liu, Z. Xu, W. Zhu, J. Fang, T. Ai, R. Tian, L. Zhang, D. He, W. Zhang and Y. Luo, *Appl. Catal., B*, 2024, **357**, 124253.